

Short-Term Evolution and Risks of Debris Cloud Stemming from Collisions in Geostationary Orbit

Peng Shu ^a, Meng Zhao ^b, Zhen-Yu Li ^c, Wei Sun^c, Yu-Qiang Li^a,
Ya-Zhong Luo^{b,*}

^a*Yunnan Observatories, Chinese Academy of Sciences, 650216, Kunming, China*

^b*National University of Defense Technology, 410073, Changsha, China*

^c*Beijing Institute of Tracking and Telecommunications
Technology, 100094, Beijing, China*

Abstract

The increasing population of objects in geostationary orbit has raised concerns about the potential risks posed by debris clouds resulting from fragmentation. The short-term evolution and associated hazards of debris generated by collisions in the geostationary region is investigated in this study. The initial distribution of two debris clouds is modeled using a single probability density function. The combined distribution of the evolved clouds is determined by solving boundary value problems. The risks associated with these debris clouds are evaluated by calculating the instantaneous impact rate and cumulative collision probability. The probability of collisions with millimeter-sized fragments may increase to 1% within 36 hours, while the probability of collisions with fragments 5 cm or larger is approximately 10^{-5} . These findings underscore the vulnerability of the geostationary region to space traffic accidents.

*Corresponding author

Email address: luoyz@nudt.edu.cn (Ya-Zhong Luo)

Keywords: Space debris, Object breakup, Density evolution, Collision probability, Geostationary orbit

1. Introduction

The geostationary orbit is a popular orbit for communication, meteorological, and navigation satellites due to its apparent motionless. Nearly all geostationary satellites are positioned in a circular orbit with a radius of 42,164 km, making this region particularly vulnerable to space traffic accidents due to the high concentration of objects [1] and the absence of natural debris-clearing mechanisms [2]. The growing population in geostationary region raises concerns about the potential risks posed by fragments stemming from explosions and collisions, particularly following the breakup of Intelsat-33e, which remained operational in geostationary orbit until October 19, 2024 [3].

A breakup event generates a large number of fragments of varying sizes [4]. In the geostationary region, only fragments larger than 1 meter are routinely tracked by the Space Surveillance Network [5], as the sensitivity of ground-based sensors decreases significantly with distance [6]. However, small, non-trackable fragments can still cause catastrophic damage to spacecraft [7]. The collision velocity of spacecraft in geostationary orbit can reach up to 4 km/s [8], while micro-meteoroids may hit at speeds of up to 72 km/s [9].

The impact of a debris cloud is inherently global [10] as it disperses around the entire Earth. Several engineering tools have been reported by the Interagency Space Debris Coordination Committee for the risk assessment of space debris [11]. Among them, NASA's Orbital Debris Engineering

Model [12, 13] and ESA’s Meteoroid and Space Debris Terrestrial Environment Reference (MASTER) [14] are considered state-of-the-art models for their respective agencies [15]. Harbin Institute of Technology has also established a Space Debris Environment Engineering Model, which yield results comparable to MASTER-8 [16]. Most of these engineering tools treat fragments as discrete particles, with their initial states drawn from statistical distributions such as the NASA Standard Breakup Model [17], the IMPACT fragmentation model from The Aerospace Corporation[18], and the Spacecraft Breakup Model from China Aerodynamics Research and Development Center [19]. To achieve reliable results, large sample sizes and repeated simulations are necessary[20, 21], as discrete methods lack the sensitivity to capture low-probability events[22]. Consequently, the computational burden is significantly heavy.

Instead of propagating discrete particles, the continuous method propagates the probability density function of debris clouds. McInnes modeled the debris clouds using the fluid continuity equation [23]. Letizia et al. developed an analytical model to evaluate the collision risk of a single fragmentation cloud [24, 25]. Subsequently, Frey and Colombo presented a fully probabilistic framework with the continuous initial distribution derived from breakup models [26]. Giudici et al. introduced density-based methods into a complex evolutionary model to predict the space environment over 200 years [27]. Recently, Wen et al. developed an inverse mapping method that accounts for J2 perturbation, enabling the evaluation of mid-term evolutions [28]. However, simplifications in distributions and orbits are required in these models, making them less competitive for the short-term evolution which is fast-changing

and inhomogeneous.

In recent years, the idea of evaluating debris cloud with boundary value problems (BVPs) has been revived to capture the accurate distribution of short-term clouds. Healy et al. developed a BVP-based method to demonstrate the exact spatial density of tens of orbits [29, 30]. Vallado and Oltrogge introduced the Debris Risk Evolution and Dispersal tool of the Analytical Graphics, Inc.¹, which evaluates the three-dimensional distribution of an evolving debris cloud by solving Lambert problems [31, 32]. Shu et al. presented the joint distribution of positions and velocities of a fragmentation cloud, and derived the impact risk from this distribution [33, 34]. Parigini et al. applied the automatic domain splitting technique to reduce the computational cost of calculating collision probability over time [35].

In this work, the BVP-based methods were enhanced by representing two clouds as a single probability density function. The initial density function was derived from NASA Standard Breakup Model as continuous functions, and the summed distribution was propagated by solving boundary value problems. The remainder of this paper is organized as follows. Section 3 derives the initial distribution of two debris clouds. The evolution of the debris cloud is described in Section 4. The hazards posed by the two debris clouds in the geostationary region are evaluated in Section 5. Finally, conclusions are drawn in Section 6.

¹Its current name is Ansys Government Initiatives.

2. Problem Statement

By 2024, over 1,000 objects have been observed near the geostationary orbit (GEO) ². The longitude and inclination of these objects are shown in Figure 1. Nearly all objects exhibit inclinations of less than 15 degrees, with the majority having inclinations of less than 1 degree. Once a fragmentation event occurs, the GEO objects will be exposed to considerable risks, as they are densely clustered along a single ring above the Equator.

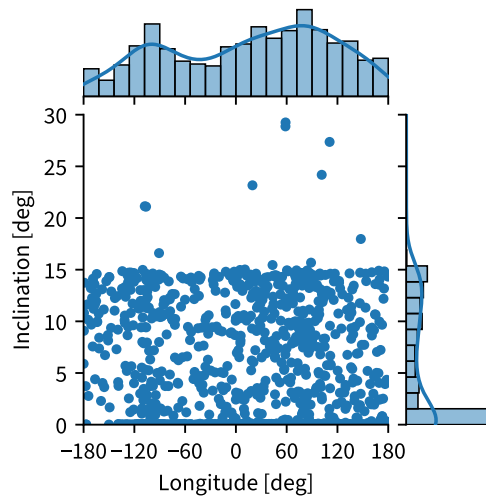


Figure 1: The distribution of the longitude and inclination of GEO objects.

Consider a collision of two objects at position \mathbf{r}_1^* at epoch t_1 , resulting in an instantaneous fragmentation event that generates two debris clouds, as shown in Figure 2. Our objective is to determine how these clouds spread and the associated risk to other GEO objects.

²Orbit elements downloaded from www.space-track.org with mean motion between [0.99,1.01] and eccentricity less than 0.01.

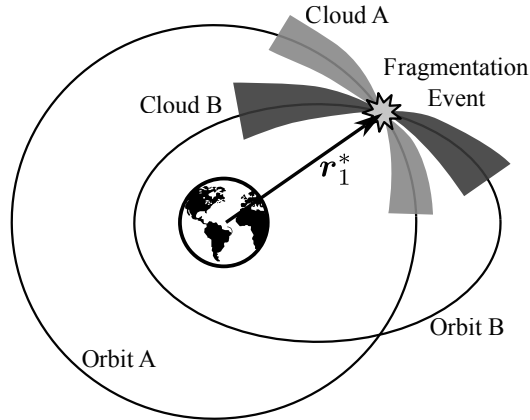


Figure 2: Illustration of fragmentation events.

3. Initial Distributions of Fragmentation Clouds

3.1. The Initial PDF of A Fragment

Consider a randomly selected fragment within the clouds, with its initial position denoted as \mathbf{r}_1 . Since all fragments are ejected from a single point, the probability density function (PDF) of \mathbf{r}_1 can be represented using the Dirac delta function [34]:

$$p_{\mathbf{r}_1}(\mathbf{r}_1) = \delta(\mathbf{r}_1 - \mathbf{r}_1^*) \quad (1)$$

where $\delta(x)$ is the Dirac delta function satisfying

$$\int_{-\infty}^{+\infty} \delta(x) dx = 1$$

$$\delta(x) = 0 \quad \text{if } x \neq 0 \quad (2)$$

The initial velocity of the fragment can be obtained by adding the ejection velocity to that of its parent object,

$$\mathbf{v}_1 = \mathbf{v}_0 + \Delta \mathbf{v} \quad (3)$$

where \mathbf{v}_0 represents the parent object's velocity, and $\Delta\mathbf{v}$ denotes the ejection velocity. The probability density function of the initial velocity can then be expressed as

$$p_{\mathbf{v}_1}(\mathbf{v}_1) = \frac{N_a}{N_a + N_b} p_{\Delta\mathbf{v}a}(\mathbf{v}_1 - \mathbf{v}_{a0}) + \frac{N_b}{N_a + N_b} p_{\Delta\mathbf{v}b}(\mathbf{v}_1 - \mathbf{v}_{b0}) \quad (4)$$

where N_a and N_b are the number of fragments in clouds A and B, respectively. $p_{\Delta\mathbf{v}a}$ and $p_{\Delta\mathbf{v}b}$ are the PDF of the ejection velocity of two clouds, which can be derived from breakup models (Sec.3.2).

Thus, the PDF of the initial state can be obtained by combining the PDFs of the position and velocity:

$$p_{\mathbf{r}_1, \mathbf{v}_1}(\mathbf{r}_1, \mathbf{v}_1) = \delta(\mathbf{r}_1 - \mathbf{r}_1^*) p_{\mathbf{v}_1}(\mathbf{v}_1) \quad (5)$$

3.2. The Distribution of Ejection Velocity

The NASA Standard Breakup Model (SBM) is a widely used model for predicting the initial distribution of fragmentation clouds [20, 24, 26, 27, 29]. It comprises a set of simple empirical equations that describe the size, area-to-mass ratio, and ejection velocity of the generated fragments, yielding highly reliable statistical results in catastrophic fragmentation scenarios [36]. This simplification ignores the effects of factors such as impact direction, material properties, and structural characteristics [37]. Recently, the University of Padova developed the Collision Simulation Tool (CST) to numerically evaluate in-space fragmentation events[36]. This tool models colliding objects with a mesh of macroscopic elements, allowing for the simulation of complex impact configurations. Nonetheless, the focus of this paper is to assess the consequences of general catastrophic collisions in geostationary orbits,

rather than being specific to particular spacecraft structures and materials. Consequently, the NASA SBM is employed in the subsequent analysis.

3.2.1. Conditional Probability Functions of NASA SBM

In typical applications, breakup models are employed to generate a large number of discrete sample fragments, with initial states following specific statistical distributions. In contrast, our approach seeks a continuous distribution function that facilitates analytical transformation.

In NASA SBM, the number of fragments with characteristic length larger than L_c is

$$N(L > L_c) = kL_c^{-\beta} \quad (6)$$

where k and β are unitless parameters determined by the type of fragmentation and parent objects. The PDF of L in the interval $[L_{\min}, L_{\max}]$ can then be derived as [26]:

$$p_L(L) = \beta \frac{L^{-(\beta+1)}}{L_{\min}^{-\beta} - L_{\max}^{-\beta}} \quad (7)$$

where L_{\max} and L_{\min} represent the upper and lower bounds of the characteristic lengths, respectively. The distribution of further parameters in NASA SBM are usually expressed with the logarithm of characteristic length $\lambda = \log_{10}(L)$, which PDF can be written as

$$p_\lambda(\lambda) = \ln(10)10^\lambda p_L(10^\lambda) \quad (8)$$

The area-to-mass ratio A/m of a fragment is determined by a conditional PDF:

$$p_{\chi|\lambda}(\chi, \lambda) = \alpha(\lambda)\mathcal{N}(\mu_1(\lambda), \sigma_1^2(\lambda)) + (1 - \alpha(\lambda))\mathcal{N}(\mu_2(\lambda), \sigma_2^2(\lambda)) \quad (9)$$

where $\chi = \log_{10}(A/m)$, \mathcal{N} is the PDF of the normal distribution, and the functions μ_1 , σ_1 , μ_2 , σ_2 and α are determined by the type of parent object.

The ejection velocity Δv is also determined by a conditional PDF in NASA SBM:

$$p_{u|\chi}(u, \chi) = \mathcal{N}(\mu_u(\chi), \sigma_u^2(\chi)) \quad (10)$$

where $u = \log_{10}(\Delta v)$ and the functions μ_u and σ_u are determined by the type of fragmentation.

3.2.2. The Distribution of Directional Ejection Velocity

The marginal distribution of u can then be calculated by integrating Eqs. (8)-(10):

$$p_u(u) = \int_{\chi_{\min}}^{\chi_{\max}} p_{u|\chi}(u, \chi) \int_{\lambda_{\min}}^{\lambda_{\max}} p_{\chi|\lambda}(\chi, \lambda) p_\lambda(\lambda) d\lambda d\chi \quad (11)$$

where λ_{\min} , λ_{\max} , χ_{\min} and χ_{\max} are determined based on the boundaries of the characteristic lengths and the area-to-mass ratio.

Then the PDF of the ejection velocity can be derived as

$$p_{\Delta v}(\Delta v) = \frac{p_u(\log_{10} \Delta v)}{\ln(10)\Delta v} \quad (12)$$

The NASA SBM assumes that the direction of the ejection velocity is uniformly distributed in space, so the PDF of the directional ejection velocity is

$$p_{\Delta \mathbf{v}}(\Delta \mathbf{v}) = \frac{p_{\Delta v}(\Delta v)}{4\pi(\Delta v)^2} \quad (13)$$

where $\Delta v = \|\Delta \mathbf{v}\|$.

3.3. Numerical Results

Jupiter 3 (also known as EchoStar 24), with a mass of 9,200 kg, is currently the heaviest satellite in GEO. Its launch requires a Falcon Heavy rocket. We consider a hypothetical collision between the upper stage of the Falcon rocket and EchoStar. The parameters of both objects prior to the collision are provided in Table 1, where "RB" refers to the rocket body and "SC" refers to the spacecraft.

For simplicity, we define the length unit as $LU = 42,164$ km which corresponds to the radius of the breakup point, and the time unit as $TU = \sqrt{LU^3/\mu}$, where μ is Earth's gravitational parameter. Consequently, the velocity unit becomes $VU = LU/TU$, and the fragmentation point is located at $\mathbf{r}_1^* = (1, 0, 0)$ LU. Additionally, the longitude of the spacecraft's sub-satellite point at the time of fragmentation is set to 0 degrees.

Table 1: Parameters of the collision objects.

Object	SC	RB
Mass (kg)	9,200	20,000
Semi-major axis (km)	42,164	11,530
Eccentricity	0.0	0.728
Inclination (deg)	0	28.5
Right ascension of ascending node (deg)	180	0
Argument of latitude (deg)	0	180
True anomaly (deg)	180	180

In this scenario, the relative kinetic energy of the collision is 778 J/g, exceeding the 40 J/g threshold for catastrophic fragmentation [17]. A sub-

stantial number of fragment samples are then generated using a validated implementation³ of the NASA SBM [38]. These discrete samples are subsequently compared with the continuous probability density function (PDF). The number of fragments in each size category is detailed in Table 2.

Table 2: The number of fragments by size category.

L , m	N_a (SC)	N_b (RB)
0.05 - 1.00	1.174×10^4	2.552×10^4
0.01 - 0.05	1.733×10^5	3.768×10^5
0.001 - 0.05	9.309×10^6	2.024×10^7

Figure 3 presents the PDF of ejection velocity categorized by size. Panels (a)-(c) illustrate the fragment distribution related to RB, whereas panels (d)-(f) depict fragments associated with SC. The histogram represents the statistical distribution of discrete samples, and the solid line represents the continuous PDF as defined by Eq. (11). The figure demonstrates a strong agreement between the two methods. In each panel, μ and σ denote the mean and standard deviation, respectively, derived from the fragment samples. The ejection velocity distribution varies substantially across size ranges, with a marked difference in larger size intervals, where fewer fragments are generated and the distributions from different parent types are notably distinct.

The distribution of directional ejection velocities for each object is calculated using Eq. (13). Subsequently, the summed PDF of the two clouds is determined according to Eq. (4), as illustrated in Figure 4. The symbol "×" denotes the velocity of SC prior to fragmentation, while "+" represents

³<https://github.com/esa/NASA-breakup-model-cpp>

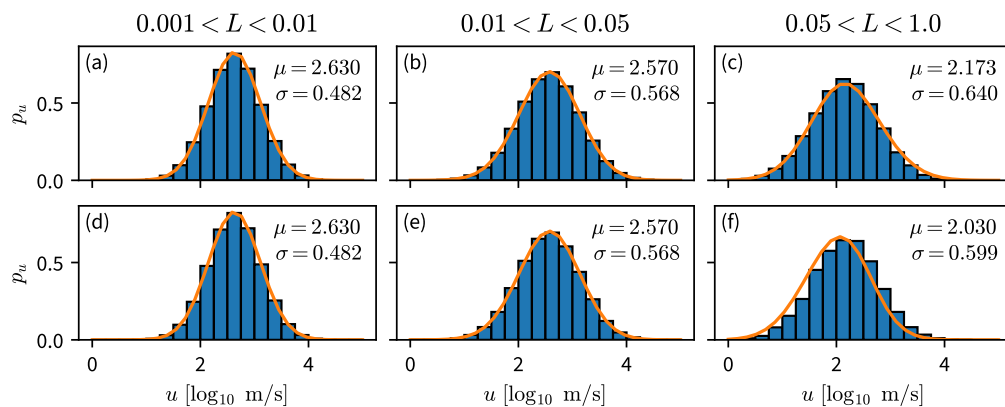


Figure 3: The distribution of ejection velocities by size category.

the velocity of RB. The probability density is notably higher in the region near the velocity of the parent bodies. The summed PDF is continuous and smooth, allowing it to be directly employed to form the initial state distribution of any number of fragments, as outlined in Eq. (5).

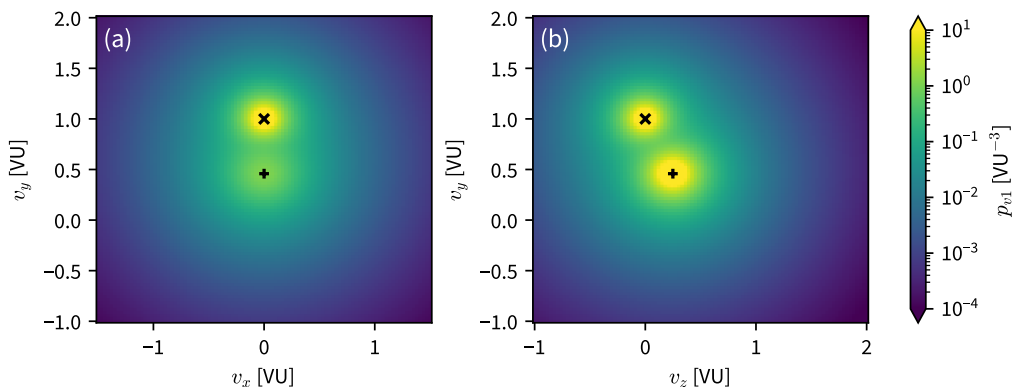


Figure 4: The summed PDF of the directional initial velocity.

4. Evolution of the Cloud Distribution

4.1. The PDF of Fragment State

After fragmentation, the fragments spread out in new orbits. After a time t , the position and velocity of a fragment become

$$\begin{aligned}\mathbf{r}_2 &= \varphi_r(t, \mathbf{r}_1, \mathbf{v}_1) \\ \mathbf{v}_2 &= \varphi_v(t, \mathbf{r}_1, \mathbf{v}_1)\end{aligned}\tag{14}$$

where φ_r and φ_v are related to the orbital dynamics.

The PDFs of \mathbf{r}_2 and \mathbf{v}_2 can then be derived by the transformation of variables:

$$p_{\mathbf{r}_2, \mathbf{v}_2}(\mathbf{r}_2, \mathbf{v}_2) = p_{\mathbf{r}_1, \mathbf{v}_1}(\varphi_r^{-1}(t, \mathbf{r}_2, \mathbf{v}_2), \varphi_v^{-1}(t, \mathbf{r}_2, \mathbf{v}_2)) \left| \det \left(\frac{\partial(\mathbf{r}_2, \mathbf{v}_2)}{\partial(\mathbf{r}_1, \mathbf{v}_1)} \right) \right|^{-1}\tag{15}$$

By exploiting the properties of δ function, this equation can be further simplified to [34]:

$$p_{\mathbf{r}_2, \mathbf{v}_2}(\mathbf{r}_2, \mathbf{v}_2) = \sum_{i=1}^m \delta(\mathbf{v}_2 - \mathbf{v}_{2i}^*) p_{\mathbf{v}_1}(\varphi_v^{-1}(t, \mathbf{r}_2, \mathbf{v}_2)) \left| \det \left(\frac{\partial \mathbf{r}_2}{\partial \mathbf{v}_1} \right) \right|^{-1}\tag{16}$$

where

$$\mathbf{v}_{2i}^* \in \{\mathbf{v}_2 \mid \varphi_r^{-1}(t, \mathbf{r}_2, \mathbf{v}_2) - \mathbf{r}_1^* = 0\}\tag{17}$$

involves solving a boundary value problem.

4.2. The Marginal Distribution of Fragment Position

Then, the marginal distribution of fragment positions can be directly integrated as:

$$\begin{aligned}
p_{\mathbf{r}_2}(\mathbf{r}_2) &= \int_{\mathbb{R}^d} p_{\mathbf{r}_2, \mathbf{v}_2}(\mathbf{r}_2, \mathbf{v}_2) d\mathbf{v}_2 \\
&= \sum_{i=1}^m \int_{\mathbb{R}^d} \delta(\mathbf{v}_2 - \mathbf{v}_{2i}^*) p_{\mathbf{v}_1}(\varphi_v^{-1}(t, \mathbf{r}_2, \mathbf{v}_2)) \left| \det \left(\frac{\partial \mathbf{r}_2}{\partial \mathbf{v}_1} \right) \right|^{-1} d\mathbf{v}_2 \\
&= \sum_{i=1}^m p_{\mathbf{v}_1}(\varphi_v^{-1}(t, \mathbf{r}_2, \mathbf{v}_{2i}^*)) \left| \det \left(\frac{\partial \mathbf{r}_2}{\partial \mathbf{v}_1} \right) \right|^{-1}
\end{aligned} \tag{18}$$

This equation can be written as

$$p_{\mathbf{r}_2}(\mathbf{r}_2) = \sum_{i=1}^m p_{\mathbf{r}_2, i}(\mathbf{r}_2) \tag{19}$$

where

$$p_{\mathbf{r}_2, i}(\mathbf{r}_2) = p_{\mathbf{v}_1}(\varphi_v^{-1}(\mathbf{r}_2, \mathbf{v}_{2i}^*)) \left| \det \left(\frac{\partial \mathbf{r}_2}{\partial \mathbf{v}_1} \right) \right|^{-1} \tag{20}$$

is the density attributed to the i -th solution of Eq. (17).

Finally, we can calculate the density of fragments at position \mathbf{r}_2 at time t :

$$n_{\mathbf{r}_2} = N_f * p_{\mathbf{r}_2}(\mathbf{r}_2) \tag{21}$$

where $N_f = N_a + N_b$ is the total number of fragments.

4.3. Numerical Results

The initial distribution obtained in Sec. 3.3 is transferred using Eq. (16), and the resulting density distribution after the fragmentation of the two clusters is obtained using Eq. (18).

Figure 5 depicts the probability density of the two clouds in three-dimensional space 48 hours after the fragmentation. In this illustration, the white ball at

the center represents the Earth. The color map indicates the probability density of fragments, with yellow signifying higher density and blue indicating lower density. This image reveals the layered structure of the fragmentation cloud, which is explored in more detail in subsequent figures.

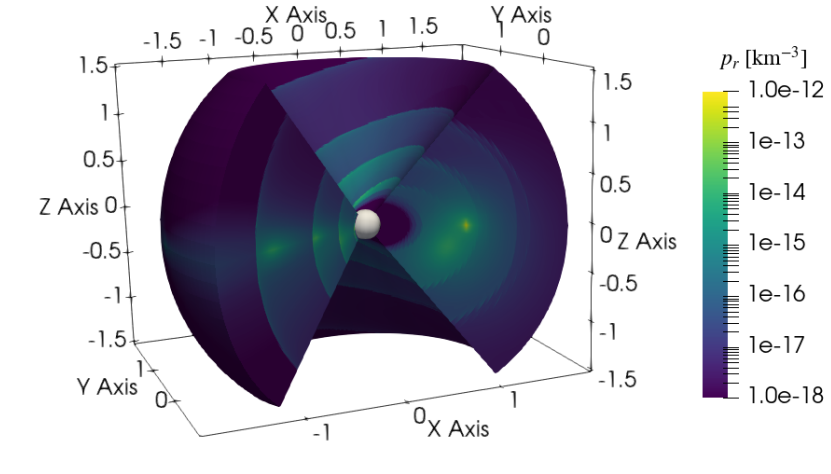


Figure 5: The 3D view of probability density.

Figures 6 and 7 present the probability density in the XY and YZ planes, respectively. The green circle at the origin represents Earth, consistent with Fig.5. Panels (a)-(f) correspond to 0.5, 1, 2, 3, 5, and 7 days after fragmentation.

Figure 6 clearly shows a pinch point on the right side of the Earth, exactly where the collision of the two objects occurs. After 0.5 days, the majority of the fragments have dispersed to the opposite side of the fragmentation point, while a small number have returned to the original location. After 7 days, the fragments have spread out to a larger area, forming several complete rings around Earth. A high-density linear region was observed on the opposite

side of the fragmentation point. This is due to the fact that the orbital plane of any fragment will necessarily contain the initial position vector \mathbf{r}_1^* .

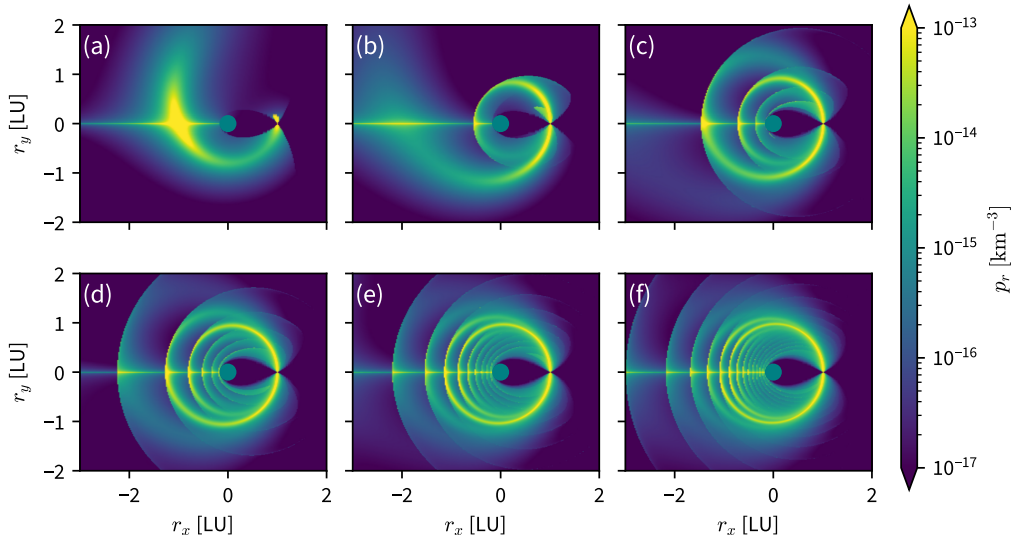


Figure 6: The evolution of density in XY plane.

Figure 7 illustrates the density distribution in the YZ plane, revealing the inclination patterns of the fragments. Over time, the debris cloud has separated into two distinct clusters in terms of inclination. One cluster, located in the equatorial plane, primarily consists of fragments from SC. The other cluster, near an inclination of 28 degrees, is mainly composed of fragments from RB. Moreover, the multi-layered structure of the debris cloud is also clearly visible in the YZ plane.

5. Risks of the Evolving Debris Clouds

The evolving debris cloud has the potential to collide with spacecraft in neighboring orbits, posing significant risks, including potentially fatal conse-

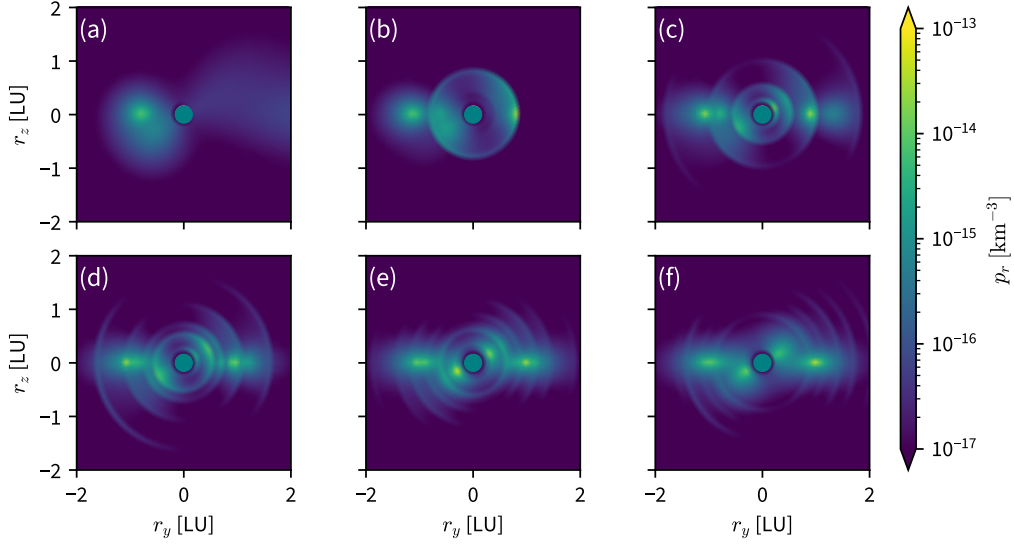


Figure 7: The evolution of density in YZ plane.

quences. To assess the collision risks, we need to calculate the probability of collision between the debris cloud and a spacecraft.

5.1. Cumulative Collision Probability

Assuming that the position and velocity of a spacecraft are \mathbf{r}_s and \mathbf{v}_s , respectively, the impact flux it suffers can be calculated from the debris density and velocity [34]:

$$\begin{aligned}
 F_{\text{in}} &= N_f \int_{\mathbb{R}^d} (\mathbf{v}_2 - \mathbf{v}_s) p_{\mathbf{r}_2, \mathbf{v}_2}(\mathbf{r}_s, \mathbf{v}_2) d\mathbf{v}_2 \\
 &= N_f \sum_{i=1}^m (\mathbf{v}_{2i}^* - \mathbf{v}_s) p_{\mathbf{r}_2, i}(\mathbf{r}_s)
 \end{aligned} \tag{22}$$

Then the impact rate to the spacecraft is

$$\dot{\eta}(t) = A_c F_{\text{in}} \tag{23}$$

where A_c is the cross-section area, and $\dot{\eta}$ means the number of impacts per unit time.

At last, we can evaluate the probability of collision between the debris cloud and the spacecraft over a given time interval:

$$P_c = 1 - e^{-\eta} \quad (24)$$

where

$$\eta = \int_0^t \dot{\eta}(t) dt \quad (25)$$

represents the cumulative number of impacts.

5.2. Numerical Results

The evolved distribution of clouds is then used to calculate the impact risk to spacecraft in GEO. The risks associated with fragments of different sizes are calculated separately, based on the number and velocity distribution detailed in Section 3.3.

Figure 8 shows the impact rate to GEO spacecraft located at different longitude over 7 days. Panels (a) - (c) correspond size intervals of 5 cm to 1 m, 1 cm to 5 cm, and 1 mm to 1 cm, respectively. As expected, the impact rate decreases for larger fragments due to their lower abundance (see Table 2). The impact rate is significantly higher near the fragmentation point and declines with increasing longitude. Despite this, the trend of the impact rate over time remains consistent. The high impact rates are observed every second orbital period. Spacecraft positioned east of the fragmentation point experience impacts sooner, as they are located ahead of the flight path of most fragments.

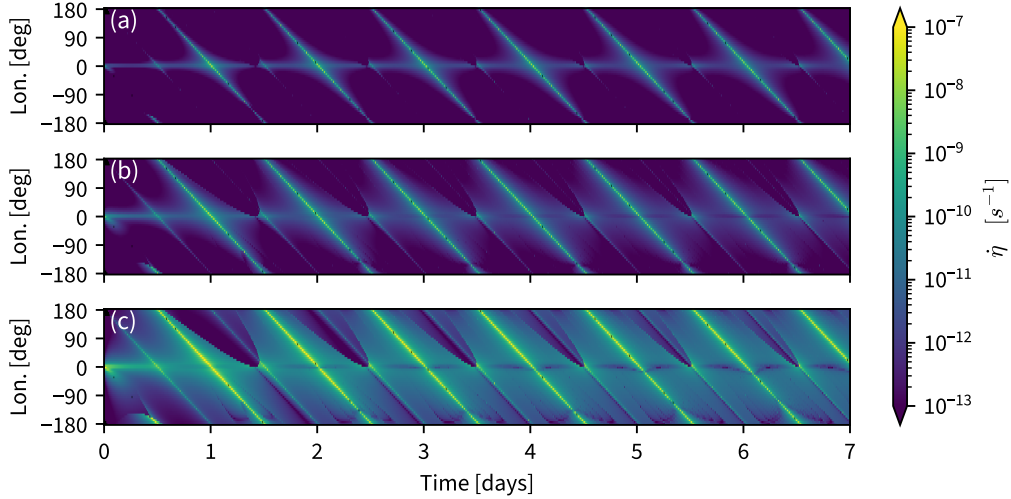


Figure 8: The Impact Rate of a Spacecraft in GEO

Figure 9 shows the cumulative collision probability of spacecraft at different longitudes. Within 1.5 days, the probability of a collision with millimeter-sized fragments increases to 10^{-3} at most locations, while the probability of a collision with fragments of 5 cm or larger is approximately 10^{-6} . Subsequently, the collision probability increases slowly because the impact rate is very low relative to P_c .

Figure 10 shows the cumulative collision probability for spacecraft across various longitudes and inclinations. Only inclinations below 15 degrees are considered, as the majority of GEO objects fall within this range. The probability of collision decreases significantly for spacecraft at higher inclinations compared to those at lower inclinations. This difference arises because the fragments are primarily ejected from two parent orbits: those from the SC are concentrated in the equatorial plane, while those from the RB are mainly distributed along the 28.5-degree inclination plane (see Figure 7). However,

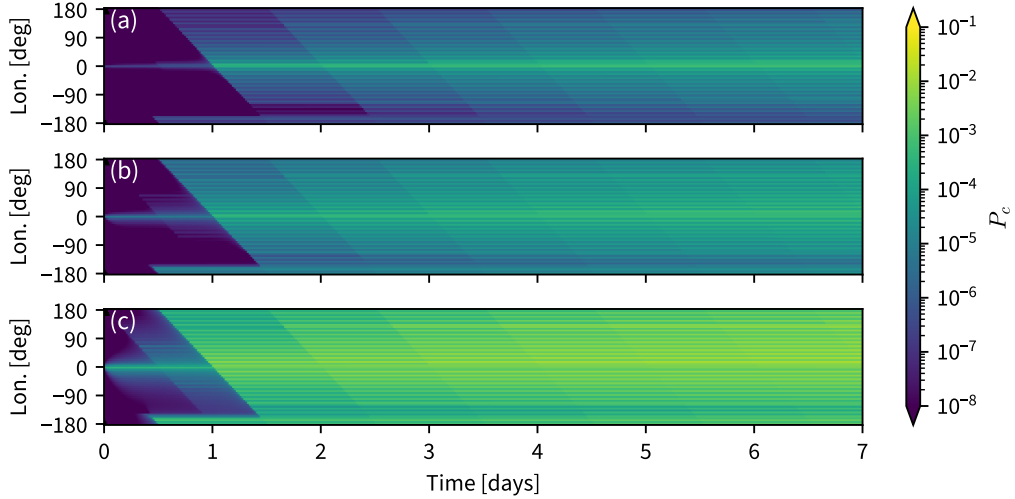


Figure 9: The Cumulative Collision Probability of a Spacecraft in GEO

exceptions occur at 0 and 180 degrees longitude, where the collision probability remains high even at higher inclinations. This can be attributed to the high density of fragments near the fragmentation point and along the diametrically opposite line.

6. Conclusions

The short-term risk of debris clouds resulting from collision events in geostationary orbit was investigated. The continuous distribution function of ejection velocities was integrated using the NASA Standard Breakup Model, and the initial distribution of the resulting two clouds was presented in a single probability density function. A strong agreement was observed between this continuous density function and the discrete samples generated by an validated implementation of the breakup model. The three-dimensional distribution of the clouds exhibited a layered structure, with a high-density

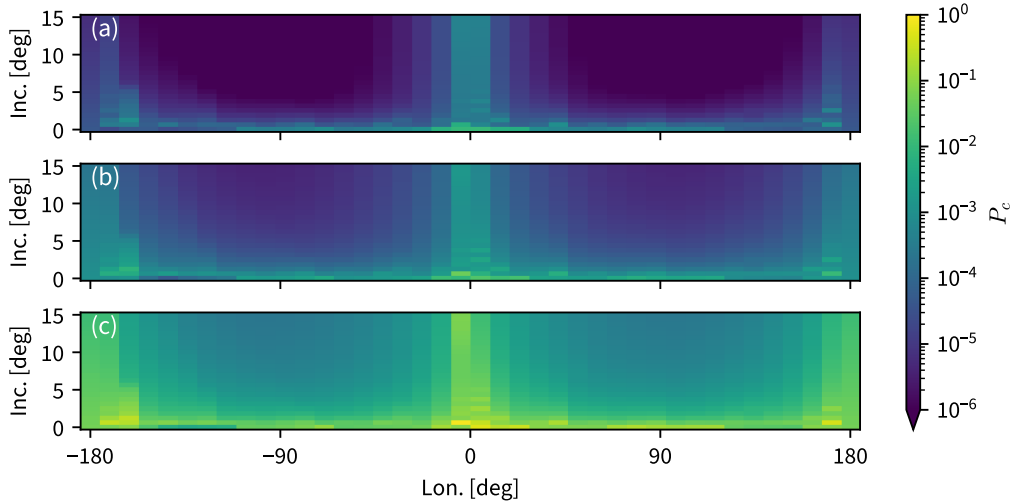


Figure 10: The Cumulative Collision Probability of a Spacecraft in GEO with Inclination

linear region opposite the fragmentation point. The risk to geostationary spacecraft at various longitudes and inclinations was also evaluated. Numerical results indicated that objects east of the fragmentation point would encounter debris impacts sooner. The probability of collision with millimeter-sized fragments may increase to 1 % within 36 hours, while the probability of collision with fragments of 5 cm or larger will approximate 10^{-5} . These results demonstrate the vulnerability of the densely populated geostationary region to space traffic accidents.

Declaration of competing interest

The authors declare that they have no known competing financial interests or personal relationships that could have appeared to influence the work reported in this paper.

Acknowledgements

This work was supported by the National Natural Science Foundation of China under Grant Nos. 12303082, 12432017, and 12402048. Peng Shu also acknowledges support from the China Postdoctoral Science Foundation (CPSF) under Grant No. 2024M75349 and the Postdoctoral Fellowship Program of CPSF under Grant No. GZC20232975.

Appendix A. Probability Density and Number Density

A probability density function $p_{\mathbf{x}}$ is a non-negative Lebesgue-integrable function which satisfies the normalization condition:

$$\int_{\mathbb{R}^d} p_{\mathbf{x}}(\mathbf{x}) d\mathbf{x} = 1 \quad (\text{A.1})$$

where $\mathbf{x} \in \mathbb{R}^d$ is a d -dimensional random variable. The probability of finding \mathbf{x} within a volume V is then

$$P(\mathbf{x} \in V) = \int_V p_{\mathbf{x}}(\mathbf{x}) d\mathbf{x} \quad (\text{A.2})$$

If \mathbf{x} is the position of a fragment and V is a volume in the space, then $P(\mathbf{x} \in V)$ is the probability of finding a fragment in V .

Number density indicates the number of particles per unit volume in the vicinity of a specific location. If $n_{\mathbf{x}}$ is the number density of fragment clouds, then the number of fragments appearing in a volume V is

$$N(\mathbf{x} \in V) = \int_V n_{\mathbf{x}}(\mathbf{x}) d\mathbf{x} \quad (\text{A.3})$$

where $n_{\mathbf{x}}$ is the number density, satisfying

$$\int_{\mathbb{R}^d} n_{\mathbf{x}}(\mathbf{x}) d\mathbf{x} = N_f \quad (\text{A.4})$$

and N_f is the total number of fragments.

References

- [1] E. S. D. Office, Classification of geosynchronous objects, Technical Note GEN-DB-LOG-00211-OPS-GR, European Space Operations Centre, Darmstadt, Germany (May 2018).
- [2] H. Mei, Hybrid removal of end-of-life geostationary satellites using solar radiation pressure and impulsive thrusts, Ph.D. thesis (2022).
- [3] R. Jewett, Intelsat’s IS-33e Satellite is a ‘Total Loss’, <https://www.satellitetoday.com/connectivity/2024/10/21/intelsats-is-33e-satellite-is-a-total-loss/> (Oct. 2024).
- [4] P. D. Anz-Meador, J. Opiela, J.-C. Liou, History of On-orbit Satellite Fragmentations, 16th Edition, Tech. Rep. NASA/TP-20220019160, NASA Orbital Debris Program Office, Houston, Texas (2022).
- [5] A. M. Nafi, Practical optical survey strategies for near geostationary orbital debris, Ph.D. thesis (2020).
- [6] J. A. Blake, P. Chote, D. Pollacco, W. Feline, G. Privett, A. Ash, S. Eves, A. Greenwood, N. Harwood, T. R. Marsh, D. Veras, C. Watson, DebrisWatch I: A survey of faint geosynchronous debris, *Advances in Space Research* 67 (1) (2021) 360–370. doi:10.1016/j.asr.2020.08.008.
- [7] D. McKnight, T. Maclay, Space Environment Management: A Common Sense Framework for Controlling Orbital Debris Risk, in: *Proceedings of*

- the Advanced Maui Optical and Space Surveillance Technologies Conference, The Maui Economic Development Board, Maui, Hawaii, 2019-09-17/2019-09-20, pp. 1–8.
- [8] D. L. Oltrogge, S. Alfano, C. Law, A. Cacioni, T. S. Kelso, A comprehensive assessment of collision likelihood in Geosynchronous Earth Orbit, *Acta Astronautica* 147 (2018) 316–345. doi:10.1016/j.actaastro.2018.03.017.
- [9] C. f. t. A. o. N. O. D. Programs, N. R. Council, Limiting Future Collision Risk to Spacecraft: An Assessment of NASA’s Meteoroid and Orbital Debris Programs, National Academies Press, Washington, 2011.
- [10] A. Lawrence, M. L. Rawls, M. Jah, A. Boley, F. Di Vruno, S. Garrington, M. Kramer, S. Lawler, J. Lowenthal, J. McDowell, M. McCaughrean, The case for space environmentalism, *Nature Astronomy* 6 (4) (2022) 428–435. doi:10.1038/s41550-022-01655-6.
- [11] IADC protection manual, Tech. Rep. IADC-04-03, Interagency Space Debris Coordination Committee (2018).
- [12] M. Matney, A. Manis, P. Anz-Meador, D. Gates, J. Seago, A. Vavrin, Y.-L. Xu, The NASA Orbital Debris Engineering Model 3.1: Development, Verification, and Validation, in: International Orbital Debris Conference (IOC), Sugar Land, TX, 2019.
- [13] P. H. Krisko, The New NASA Orbital Debris Engineering Model ORDEM 3.0, in: AIAA/AAS Astrodynamics Specialist Conference, AIAA

- 2014-4227, San Diego, CA, 2014-08-04/2014-08-07. doi:10.2514/6.2014-4227.
- [14] A. Horstmann, Enhancement of S/C fragmentation and environment evolution models, Tech. Rep. DD-0045, Technische Universität of Braunschweig, Braunschweig (Aug. 2020).
- [15] P. H. Krisko, S. Flegel, M. J. Matney, D. R. Jarkey, V. Braun, ORDEM 3.0 and MASTER-2009 modeled debris population comparison, *Acta Astronautica* 113 (2015) 204–211. doi:10.1016/j.actaastro.2015.03.024.
- [16] Y. Liu, R. Chi, B. Pang, HU. Diqi, W. Cao, D. Wang, Space debris environment engineering model 2019: Algorithms improvement and comparison with ORDEM 3.1 and MASTER-8, *Chinese Journal of Aeronautics* 37 (5) (2024) 392–409. doi:10.1016/j.cja.2023.12.004.
- [17] P. H. Krisko, Proper implementation of the 1998 NASA breakup model, *Orbital Debris Quarterly News* 15 (4) (2011) 4–5.
- [18] D. L. Mains, M. E. Sorge, The IMPACT satellite fragmentation model, *Acta Astronautica* 195 (2022) 547–555. doi:10.1016/j.actaastro.2022.03.030.
- [19] T. Yao, Z. Yang, Y. Luo, S. Lan, L. Ren, Generation of initial debris cloud distributions for breakup events based on CARD-C-SBM, *Acta Astronautica* 219 (2024) 580–591. doi:10.1016/j.actaastro.2024.03.060.

- [20] D. Jang, R. Linares, Simulating the Evolution of Lethal Non-Trackable Population and its Effect on LEO Sustainability (Aug. 2024). doi:10.48550/arXiv.2408.15025.
- [21] J.-C. Liou, N. L. Johnson, Risks in Space from Orbiting Debris, *Science* 311 (5759) (2006) 340–341. doi:10.1126/science.1121337.
- [22] S.-K. Au, J. L. Beck, Estimation of small failure probabilities in high dimensions by subset simulation, *Probabilistic Engineering Mechanics* 16 (4) (2001) 263–277. doi:10.1016/S0266-8920(01)00019-4.
- [23] C. R. McInnes, An analytical model for the catastrophic production of orbital debris, *ESA Journal* 17 (4) (1993) 293–305.
- [24] F. Letizia, C. Colombo, H. G. Lewis, Analytical Model for the Propagation of Small-Debris-Object Clouds After Fragmentations, *Journal of Guidance, Control, and Dynamics* 38 (8) (2015) 1478–1491. doi:10.2514/1.G000695.
- [25] F. Letizia, C. Colombo, H. G. Lewis, Collision Probability Due to Space Debris Clouds Through a Continuum Approach, *Journal of Guidance, Control, and Dynamics* 39 (10) (2016) 2240–2249. doi:10.2514/1.G001382.
- [26] S. Frey, C. Colombo, Transformation of Satellite Breakup Distribution for Probabilistic Orbital Collision Hazard Analysis, *Journal of Guidance, Control, and Dynamics* 44 (1) (2021) 88–105. doi:10.2514/1.G004939.
- [27] L. Giudici, C. Colombo, A. Horstmann, F. Letizia, S. Lemmens, Density-based evolutionary model of the space debris environment in low-

- Earth orbit, *Acta Astronautica* 219 (2024) 115–127. doi:10.1016/j.actaastro.2024.03.008.
- [28] C. Wen, Z. Jin, C. Peng, D. Qiao, Modeling Medium-Term Debris Cloud of Satellite Breakup via Probabilistic Method, *Journal of Guidance, Control, and Dynamics* 47 (8) (2024) 1602–1619. doi:10.2514/1.G008062.
- [29] L. M. Healy, S. Kindl, E. Rolfe, C. Binz, Structure and evolution of a debris cloud in the early phases, in: *Advances in the Astronautical Sciences*, Vol. 158, Univelt, Inc., San Diego, CA, 2016, pp. 2715–2743. doi:10.5281/zenodo.1406548.
- [30] L. M. Healy, C. R. Binz, S. Kindl, Orbital Dynamic Admittance and Earth Shadow, *The Journal of the Astronautical Sciences* 67 (2) (2020) 427–457. doi:10.1007/s40295-018-00144-1.
- [31] D. A. Vallado, D. L. Oltrogge, Fragmentation Event Debris Field Evolution Using 3D Volumetric Risk Assessment, in: *7th European Conference on Space Debris*, ESA Space Debris Office, Darmstadt, Germany, 2017-04-18/2017-04-21.
- [32] D. L. Oltrogge, D. A. Vallado, Application of new debris risk evolution and dispersal (DREAD) tool to characterize post-fragmentation risk, in: *AAS/AIAA Astrodynamics Specialist Conference*, Vol. 162, 2017, pp. 463–482.
- [33] P. Shu, Z. Yang, Y.-Z. Luo, Z.-J. Sun, Collision Probability of Debris Clouds Based on Higher-Order Boundary Value Problems, *Journal of*

- Guidance, Control, and Dynamics 45 (8) (2022) 1512–1522. doi:10.2514/1.G006356.
- [34] P. Shu, Z. Yang, Y.-Z. Luo, Impact Risk of a Debris Cloud to Spacecraft, *Journal of Guidance, Control, and Dynamics* 46 (5) (2023) 989–997. doi:10.2514/1.G007056.
- [35] C. Parigini, R. Algethamie, R. Armellin, Short-Term Collision Probability Caused by Debris Cloud, *Journal of Guidance, Control, and Dynamics* 47 (5) (2024) 874–886. doi:10.2514/1.G007687.
- [36] A. Francesconi, C. Giacomuzzo, L. Olivieri, G. Sarego, M. Duzzi, F. Feltrin, A. Valmorbida, K. D. Bunte, M. Deshmukh, E. Farahvashi, J. Pervez, M. Zaake, T. Cardone, D. de Wilde, CST: A new semi-empirical tool for simulating spacecraft collisions in orbit, *Acta Astronautica* 160 (2019) 195–205. doi:10.1016/j.actaastro.2019.04.035.
- [37] L. Olivieri, C. Giacomuzzo, A. Francesconi, Numerical simulation of COSMOS 2499 fragmentation, *CEAS Space Journal* 16 (6) (2024) 659–665. doi:10.1007/s12567-024-00545-z.
- [38] J. Schuhmacher, Efficient Implementation and Evaluation of the NASA Breakup Model in modern C++, Bachelor’s Thesis, Technical University of Munich (2021).